A unified framework for the multi-scale computational homogenisation of 3D-textile composites

Z. Ullah[a,1], X. -Y. Zhou[b], L. Kaczmarczyk[c], E. Archer[a], A. McIlhagger[a], E. Harkin-Jones[a]

[a]*School of Engineering, Ulster University, Jordanstown, Newtownabbey, Antrim BT37 0QB, UK*

[b]*School of Engineering, Cardiff University, Cardiff CF24 3AA, UK*

[c]*School of Engineering, Rankine Building, The University of Glasgow, Glasgow, G12 8LT, UK*

Abstract

This paper extends the applications of a novel and fully automated multi-scale computational homogenisation framework, originally proposed by the authors (Ullah, et al. (2017)) for uni-directional and 2D-textile composites, to 3D-textile composites. 3D-textile composites offer many advantages over 2D-textile composites but their highly complicated and unpredictable post-cured geometries make their design very challenging. Accurate computational models are therefore essential to the development of these materials. The computational framework described in this paper possesses a variety of novel features which have never been tried for this class of composites and can potentially help to fully automatise and improve their design process. A unified approach is used to impose the representative volume element boundary conditions, which allows convenient switching between linear displacement, uniform traction and periodic boundary conditions. The computational framework is implemented using hierarchic basis functions of arbitrary polynomial order, which allows one to increase the order of approximation without changing the finite element mesh. The yarns' principal directions, required for the transversely isotropic material model are calculated using a potential flow analysis along these yarns. This feature is very useful for 3D-textile composites and can accurately determine fibres' directions even in the case of very deformed yarns. A numerical example from literature consisting of a 3D-orthogonal woven composite is used to demonstrate the correct implementation and performance of the developed computational framework. Also, the developed computational framework is used to perform a comparative study of the homogenised mechanical properties of five 3D-textile composites with different yarn architectures.

Keywords: 2.5D and 3D textile/woven, FRP composites, Multi-scale computational homogenisation, Finite element analysis, Transverse isotropy

---

[1]Correspondence to: Z. Ullah, E-mail: z.ullah@ulster.ac.uk

1. Introduction

Due to their exceptional mechanical and chemical properties, fibre reinforced polymer (FRP) composites are used in a variety of engineering applications including aerospace, automotive, marine, prosthetics and civil structures [1, 2]. Textile or woven composites make use of interlaced or woven fibres as reinforcement and integrate the full functionality of the textile processing industry into composite manufacturing [3]. Conventional two-dimensional textile reinforcement, e.g. plain, twill and n-harness satin architectures offer a variety of advantages including high strength, high stiffness, low density and low manufacturing cost [4]. These 2D-textile composites have outstanding in-plane mechanical properties but suffer from having very week mechanical properties in the out-of-plane direction [5–7]. 3D-textile composites have yarns oriented in x, y and z directions and therefore possess improved out-of-plane properties. As compared to conventional 2D-textile composites, 3D-textile composites possess high delamination resistance and improved impact performance [8–10]. 3D-textile composites allow manufacturing of near-net shape in a single production step leading to minimum scrap [11]. However, lower fibre volume fraction and reduced in-plane mechanical properties are limitations of 3D-textile composites [12–16]. Moreover, the associated highly complex and unpredictable geometry making their modelling more challenging.

Due to the multi-scale, complicated and heterogeneous nature of 3D-textile composites, computational homogenisation (CH) is the most appropriate computational framework for the calculation of their effective or homogenised properties [17, 18]. These homogenised properties can then be used for the analysis of macro-level structure. As compared to analytical methods [19–24], numerical techniques provide better prediction of their homogenised mechanical properties. A brief overview of the available literature on the computational homogenisation of 3D-textile composites is given here. A detailed description of a 3D Mosaic structural analysis tool is given in [25]. The developed tool was used for the calculation of homogenised mechanical properties of 3D-orthogonal composites, modelled using an idealised geometry. The simulation results were compared with experimental data and found in a good agreement. In [26], effects of the z-yarns' geometry on the homogenised mechanical properties were investigated using finite element analysis. Both crowned and un-crowned z-yarns were considered. In [27], meshfree methods based on radial basis functions and moving kriging interpolation were used for the calculation of homogenised mechanical properties of 3D-orthogonal woven composites. Results were compared with the finite element and experimental results from [25] and found in a good agreement. A finite element based procedure for calculating the effective mechanical properties of 3D-textile composites was presented in [28]. The main emphasis was on the accurate geometric modelling and the procedure was used for three weave types. Numerical results were compared with the experimental results and found to be about 10% stiffer. A discrete homogenisation scheme was used in [8] for the prediction of effective mechanical

properties of 3D dry textiles composites. Results were satisfactory compared to FEM results. A non-conformal mesh-based finite-element procedure was proposed in [29] for the calculation of thermo-mechanical properties of 2D and 3D textile composites. The procedure allowed to mesh penetrated yarns without geometrical modifications. A comparative study between periodic and free mesh for 3D braided composite was peformed in [30]. Freely generated mesh was combined with general periodic boundary condition. Predicted stiffnesses, stresses distribution, deformations and strengths by mean of free mesh unit cell agree well with those using periodic mesh. Recently in [31], a multi-scale finite element is applied to 3D-textile composites with voids in both matrix and yarns. Experiments were also conducted to verify the FE model. A comprehensive book on the woven composites has been published recently [32] dealing with the experimental, analytical and numerical studies of both 2D and 3D woven composites. A detailed computational homogenisation procedure and continuum damage model were presented in the same book and used within the framework of both finite elements and meshless methods [33]. The book also presents the experimental, analytical and numerical models for the compressive failure of woven composites [34]. Moreover, a detailed numerical procedures for the 3D woven composites both on the unit-cell and structural-level were also included [35].

In this paper, we extend the application of a novel and fully automated multi-scale CH framework to 3D-textile composites, originally proposed in the authors' previous paper, [17], for unidirectional and 2D-textile composites. The computational framework possesses a variety of novel features which are very useful in the case of 3D-textile composites. The highly complicated and unpredictable post-cured geometries associated with these composites consisting of fully deformed yarns within the matrix material making their design very challenging. On the other hand, 3D-textile composites help to fully exploit the flexibility and robustness of the computational framework. A unified approach [17, 36, 37] is used to impose the representative volume element (RVE) boundary conditions, which allows convenient switching between linear displacement, uniform traction and periodic boundary conditions. The computational framework is implemented using hierarchic basis functions of arbitrary polynomial order [38], which allows to increase the order of approximation without changing the finite element mesh. The yarns' principal directions, required for the transversely isotropic material model are calculated using a potential flow analysis along these yarns. This feature is very useful for 3D-textile composites and can accurately determine fibres' directions even in the case of very deformed yarns. The computational framework was designed to take advantage of the distributed memory high-performance computing and is implemented using PETSc [39] and MOAB [40] libraries. Both matrix and yarns are considered as homogeneous and linear elastic materials. Matrix and yarns are modelled using isotropic and transversely isotropic material models respectively. Yarns geometry are modelled with elliptical cross-sections and cubic spline paths. CUBIT/Trelis [41] and Paraview [42] are used as a pre- and post-processor respectively.

This paper is organised as follows. A detailed description of the computational framework is given in §2. The associated multi-scale CH and the corresponding imposition of RVE boundary conditions are given in §2.1. A brief overview of the calculation of yarns' principle directions, required for the transversely isotropic material model and the associated transformation of stiffness matrix from local to global coordinate axes are given in §2.2. Two numerical examples are given in §3. The first numerical example (§3.1) is chosen from the literature and used to validate the proposed computational framework. In the second numerical examples (§3.2), a comparison of the homogenised mechanical properties are made among five 3D-textile composites with 2.5D and 3D yarn architectures. Finally, concluding remarks are given in §4.

2. Computational framework

The computational framework proposed for the calculation of homogenised mechanical properties consists of multi-scale CH and the associated imposition of RVE boundary conditions. Computation of the fibres directions within yarns is also an integral part of the same framework.

2.1. Multi-scale computational homogenisation

The working principle of multi-scale CH is shown in Figure 1, where an RVE consisting of 3D arrangement of yarns is associated with each macro-level integration point $\mathbf{x} = \begin{bmatrix} x_1 & x_2 & x_3 \end{bmatrix}^T$. In Figure 1, $\Omega \subset \mathbb{R}^3$ and $\Omega_\mu \subset \mathbb{R}^3$ represents the macro- and micro-level structures respectively.
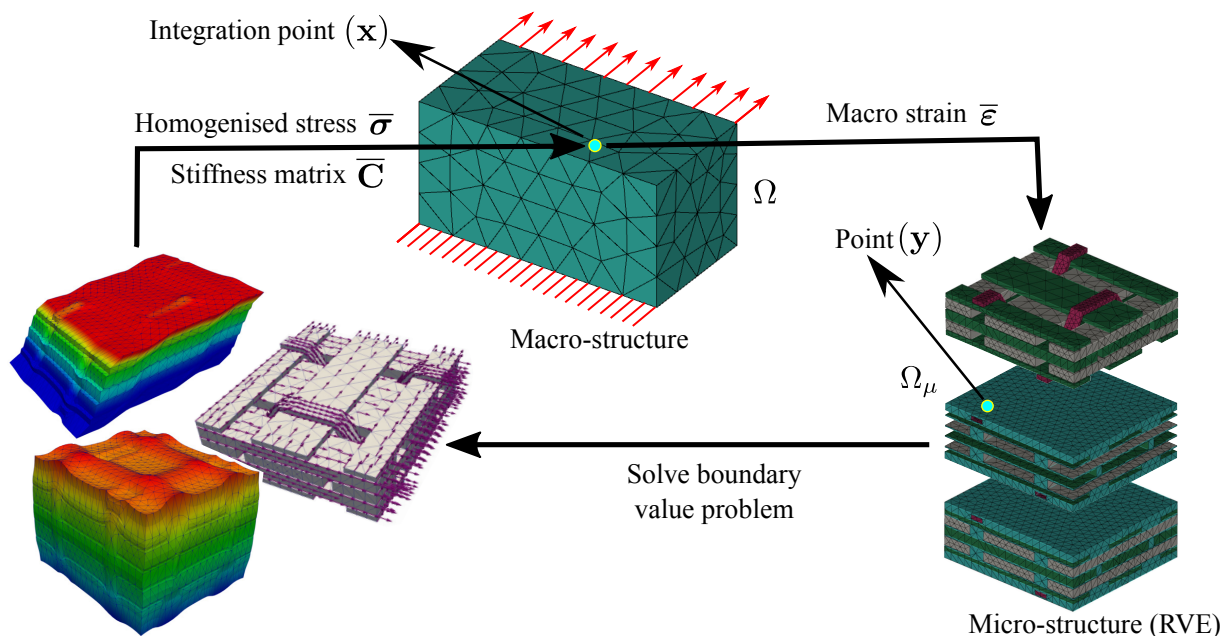

Figure 1: Multi-scale computational homogenisation.

The macro-to-micro transition consists of the construction of a micro-level boundary value problem. This step consists of formulation of RVE boundary conditions using the macro-level strain $\overline{\boldsymbol{\varepsilon}} = \begin{bmatrix} \overline{\varepsilon}_{11} & \overline{\varepsilon}_{22} & \overline{\varepsilon}_{33} & 2\overline{\varepsilon}_{12} & 2\overline{\varepsilon}_{23} & 2\overline{\varepsilon}_{31} \end{bmatrix}^T$. Solution of the RVE boundary value problem is then followed by micro-to-macro transition. This step consists of calculation of the homogenised stress $\overline{\boldsymbol{\sigma}} = \begin{bmatrix} \overline{\sigma}_{11} & \overline{\sigma}_{22} & \overline{\sigma}_{33} & \overline{\sigma}_{12} & \overline{\sigma}_{23} & \overline{\sigma}_{31} \end{bmatrix}^T$ and stiffness matrix $\overline{\mathbf{C}}$. At a point $\mathbf{y} = \begin{bmatrix} y_1 & y_2 & y_3 \end{bmatrix}^T$ on the RVE, the displacement field is written as

$$\mathbf{u}_\mu(\mathbf{y}) = \overline{\boldsymbol{\varepsilon}}(\mathbf{x})\mathbf{y} + \widetilde{\mathbf{u}}_\mu(\mathbf{y}), \tag{1}$$

where $\overline{\boldsymbol{\varepsilon}}\mathbf{y}$ and $\widetilde{\mathbf{u}}_\mu$ are linear and fluctuating displacement terms. Strain at point $\mathbf{y}$ is written as

$$\boldsymbol{\varepsilon}_\mu(\mathbf{y}) = \nabla^s \mathbf{u}_\mu = \overline{\boldsymbol{\varepsilon}}(\mathbf{x}) + \tilde{\boldsymbol{\varepsilon}}(\mathbf{y}), \tag{2}$$

consisting of macro-level strain $\overline{\boldsymbol{\varepsilon}}(\mathbf{x})$ and strain fluctuation $\tilde{\boldsymbol{\varepsilon}}(\mathbf{y})$. The volume average of the micro-level strain should give the macro-level strain, i.e.

$$\overline{\boldsymbol{\varepsilon}}(\mathbf{x}) = \frac{1}{V}\int_{\Omega_\mu} \boldsymbol{\varepsilon}_\mu(\mathbf{y})\, d\Omega_\mu = \overline{\boldsymbol{\varepsilon}}(\mathbf{x}) + \frac{1}{V}\int_{\Omega_\mu} \tilde{\boldsymbol{\varepsilon}}_\mu(\mathbf{y})\, d\Omega_\mu, \tag{3}$$

where V is the volume of the RVE. To satisfy Equation (3), the volume average of the strain fluctuation should be zero, i.e.

$$\frac{1}{V}\int_{\Omega_\mu} \tilde{\boldsymbol{\varepsilon}}_\mu(\mathbf{y})\, d\Omega_\mu = 0. \tag{4}$$

Similarly, calculation of the macro-stress $\overline{\boldsymbol{\sigma}}$ is determined by volume averaging of the micro-stress $\overline{\boldsymbol{\sigma}}_\mu$, i.e.

$$\overline{\boldsymbol{\sigma}}(\mathbf{x}) = \frac{1}{V}\int_{\Omega_\mu} \boldsymbol{\sigma}_\mu(\mathbf{y})\, d\Omega_\mu. \tag{5}$$

The strong form of the equilibrium equation for the RVE is written as

$$\text{div}(\boldsymbol{\sigma}_\mu) = \nabla \cdot \boldsymbol{\sigma}_\mu = \mathbf{0}. \tag{6}$$

Similarly, the weak form of Equation (6) is written as

$$\int_{\Omega_\mu} \boldsymbol{\sigma}_\mu(\mathbf{y}) : \nabla^s \boldsymbol{\eta}_\mu d\Omega_\mu - \int_{\partial\Omega_\mu} \mathbf{t}(\mathbf{y}) \cdot \boldsymbol{\eta}_\mu \partial\Omega_\mu = \mathbf{0}. \tag{7}$$

In Equation (7), the first term on the right hand side is known as internal virtual work and the associated second term is knows as external virtual work. $\mathbf{t}$ and $\boldsymbol{\eta}_\mu$ are applied traction and virtual displacement respectively.

According to the Hill-Mandel principle, the relation between macro- and micro-level work is

written as

$$\overline{\varepsilon} : \overline{\sigma} = \frac{1}{V} \int_{\Omega_\mu} \varepsilon_\mu : \sigma_\mu d\Omega_\mu. \tag{8}$$

Combining Equations (1), (5), (7) and (8) leads to

$$\int_{\Omega_\mu} \sigma_\mu(\mathbf{y}) : \nabla^s \boldsymbol{\eta}_\mu d\Omega_\mu = 0, \tag{9}$$

and the second term in Equation (7) vanish, i.e.

$$\int_{\partial\Omega_\mu} \mathbf{t}(\mathbf{y}) \cdot \boldsymbol{\eta} \partial\Omega_\mu = 0. \tag{10}$$

Thus, on the micro-level, the problem reduces to a calculation of the displacement fluctuation for a given macro-strain $\overline{\varepsilon}$.

The following three types of RVE boundary conditions are considered in this paper:

1. Linear boundary displacement: In this case, it is assumed that the displacement fluctuation $\widetilde{\mathbf{u}}_\mu(\mathbf{y})$ is zero over the RVE boundary. Therefore, Equation (1) is written as

$$\mathbf{u}_\mu(\mathbf{y}) = \overline{\varepsilon}(\mathbf{x})\mathbf{y}, \qquad \forall \mathbf{y} \in \partial\Omega_\mu. \tag{11}$$

   This leads to fully prescribed displacement on the RVE boundary.
2. Periodic boundary conditions: In this case displacement and traction are assumed to be periodic and anti-periodic respectively, i.e.

$$\left. \begin{array}{l} \tilde{\mathbf{u}}_\mu(\mathbf{y}^+) = \tilde{\mathbf{u}}_\mu(\mathbf{y}^-) \\ \mathbf{t}(\mathbf{y}^+) = -\mathbf{t}(\mathbf{y}^-) \end{array} \right\} \qquad \forall \text{ pairs} \left\{ \mathbf{y}^+, \ \mathbf{y}^- \right\}, \tag{12}$$

   here, $\mathbf{y}^+ \in \partial\Omega_\mu^+$ and $\mathbf{y}^- \in \partial\Omega_\mu^-$ are two opposite points on the RVE boundary.
3. Uniform traction boundary conditions: In this case the traction on the RVE boundary is prescribed using the macro-level stress $\overline{\sigma}$, i.e.

$$\mathbf{t} = \overline{\sigma} \cdot \mathbf{n}, \tag{13}$$

   here $\mathbf{n}$ represents normal to the RVE boundary.

These three types of RVE boundary conditions generate different RVE behaviour. The linear displacement boundary conditions generate the stiffest RVE response. On the other hand, the traction boundary condition leads to a least kinematically constrained response. The response of the periodic boundary conditions lies between the displacement and traction boundary conditions. In this paper, the RVE boundary conditions are implemented in a unified manner

[17, 36, 37] within the framework of hierarchic basis functions [38] using distributed memory high-performance computing. The discretised system of equations are written as:

$$\begin{bmatrix} \mathbf{K} & \mathbf{C}^T \\ \mathbf{C} & \mathbf{0} \end{bmatrix} \begin{Bmatrix} \mathbf{u} \\ \boldsymbol{\lambda} \end{Bmatrix} = \begin{Bmatrix} \mathbf{0} \\ \mathbf{D}\overline{\boldsymbol{\varepsilon}} \end{Bmatrix}, \tag{14}$$

here $\mathbf{K}$ is the stiffness matrix and $\mathbf{u}$ is the a vector of unknown displacements. Moreover, $\boldsymbol{\lambda}$ is an unknown vector of Lagrange multipliers and Matrices $\mathbf{C}$ and $\mathbf{D}$ are calculated over the RVE boundary and are given as

$$\mathbf{C} = \int_{\partial\Omega_\mu} \mathbf{H}\mathbf{N}^T\mathbf{N}d\partial\Omega_\mu, \qquad \mathbf{D} = \int_{\partial\Omega_\mu} \mathbf{H}\mathbf{N}^T\mathbf{X}d\partial\Omega_\mu. \tag{15}$$

A detailed description of matrices $\mathbf{N}$, $\mathbf{X}$ and $\mathbf{H}$ are given in [17, 36, 37] and is not repeated here. Finally, homogenised stress is calculated from the resulted Lagrange multipliers $\boldsymbol{\lambda}$ using

$$\overline{\boldsymbol{\sigma}} = \frac{1}{V}\mathbf{D}^T\boldsymbol{\lambda}. \tag{16}$$

Similarly, the homogenised stiffness matrix $\mathbf{C}$, which relates the macro-level stress $\overline{\boldsymbol{\sigma}}$ and strain $\overline{\boldsymbol{\varepsilon}}$, is calculated by solving six RVE problems subjected to six unit strains leading to

$$\overline{\mathbf{C}} = \begin{bmatrix} \overline{\boldsymbol{\sigma}}^1 & \overline{\boldsymbol{\sigma}}^2 & \overline{\boldsymbol{\sigma}}^3 & \overline{\boldsymbol{\sigma}}^4 & \overline{\boldsymbol{\sigma}}^5 & \overline{\boldsymbol{\sigma}}^6 \end{bmatrix}, \tag{17}$$

where for example:

$$\begin{aligned} \overline{\boldsymbol{\sigma}}^1 : & \quad \text{for } \overline{\boldsymbol{\varepsilon}} = \begin{bmatrix} 1 & 0 & 0 & 0 & 0 & 0 \end{bmatrix}^T \\ \overline{\boldsymbol{\sigma}}^4 : & \quad \text{for } \overline{\boldsymbol{\varepsilon}} = \begin{bmatrix} 0 & 0 & 0 & 1 & 0 & 0 \end{bmatrix}^T \end{aligned}. \tag{18}$$

Finally, mechanical properties including Young's moduli, shear moduli and Poisson's ratios can be calculated using the procedure described in §Appendix A.

2.2. Yarns directions

In this paper, yarns are considered as unidirectional composites, consisting of fibre bundle in a polymer matrix and are modelled as homogeneous and transversely isotropic materials. Five elastic constants are required to fully describe the material behaviour of yarns on the meso-level. These material constants are $E_p, \nu_p, E_z, \nu_{pz}$ and G_{zp}, where p and z are transverse and axial directions respectively as shown in Figure 2.

The global stiffness matrix $\mathbf{K}$, given in Equation (14), consists of contributions from both matrix and yarns. Transformation of the local stiffness matrix is required at each integration point associated with yarns from local to global coordinates. The local coordinate system here
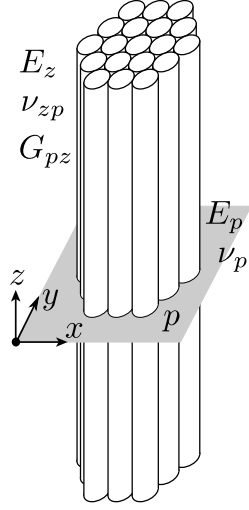
Figure 2: Transversely isotropic material model.

is associated with the integration point while global coordinates are associated with the RVE. In order to perform this transformation, the yarns direction needs to be calculated at each of these points. In this paper, a similar approach based on the potential flow theory, as described in our previous publication [17, 18, 37], is used for the calculation of yarns' directions. Yarns are considered as pipes and the potential flow problem is solved through each of them in turn. The strong form of governing equation for the potential flow is written as

$$\nabla^2\phi = \frac{\partial^2\phi}{\partial x^2} + \frac{\partial^2\phi}{\partial y^2} + \frac{\partial^2\phi}{\partial z^2} = 0, \tag{19}$$

where ϕ is the potential field. The gradient of the potential field is a velocity vector $\nabla\phi = \mathbf{v}$, which can be considered as the direction of yarns. The different processes involved in the manufacturing of 3D-textile composites result in deformed yarns consisting of variable cross-sections along their lengths. Therefore, the aforementioned approach is the most appropriate way to determine their directions. Application of this approach to more complicated cases is also demonstrated in [43].

Finally, the following expression is used to transfer the local stiffness matrix $\mathbf{C}_{\text{loc}}$ into global stiffness matrix $\mathbf{C}_{\text{glob}}$

$$\mathbf{C}_{\text{glob}} = \mathbf{T}_\sigma \mathbf{C}_{\text{loc}} \mathbf{T}_\sigma^T = \mathbf{T}_\varepsilon^{-T} \mathbf{C}_{\text{loc}} \mathbf{T}_\varepsilon^{-1}, \tag{20}$$

here $\mathbf{T}_\sigma$ and $\mathbf{T}_\varepsilon$ are coordinate transformation matrices for stress and strain respectively, the details of which are given in [44].

3. Numerical Examples

Two numerical examples are presented now to demonstrate the correct implementation and performance of the developed computational framework. The first numerical example is used to validate the computational framework against already existing results available in the literature. In the second numerical example, a comparison is made among the homogenised mechanical properties of five 3D-textile composites with different yarn architectures.

3.1. 3D orthogonal woven composite with straight-edge yarns

The first numerical example consists of a 3D-textile composite with through-the-thickness, orthogonal yarns architecture. The same example is also given [25, 27, 45], which is used here for validation of the proposed computational framework. A detailed RVE for this example is shown in Figure 3. A 3D orthogonal woven fabric is shown in Figure 3(a). An RVE consisting of both matrix and yarns is shown in Figure 3(b). Figures 3(c) and 3(d) show a separate view of the matrix and yarns respectively. Binder yarns are also shown in Figure 3(e). Yarns geometry is assumed to be oversimplified consisting of rectangular cross-sections. Similarly, in the thickness direction, binder yarns are modelled as broken lines consisting of two inclined and one vertical section. In this case, the RVE consists of two layers of warp yarns and three layers of weft yarns. In [25, 27, 45], the RVE geometry was modified to account for the indentation of the binder yarns into the weft yarns. In addition, warp segments of the binder yarns and the associated top and bottom matrix layers were removed. These geometrical modifications help in removing extra matrix material leading to a fibre volume fraction of 49% which is equivalent to the experimentally observed value. The experimental fibre volume fraction in the yarns and RVE are 60% and 49% respectively. These modification leads to non-periodic geometry and mesh in the thickness direction.

In the proposed computational framework, periodic geometry and mesh are prerequisites to impose the periodic boundary condition on the RVE. In this paper, we are analysing two cases, i.e. one with the original RVE (shown in Figure 3(b)) and one with the same modifications as suggested in [25, 27, 45] (shown in Figure 4(a)). The original periodic RVE allows to use linear displacement, periodic and uniform traction boundary conditions while the modified non-periodic RVE only allows to impose the linear displacement and uniform traction boundary conditions. The original RVE has a very low fibre volume fraction of 31.0% while the modified RVE has a fibre volume fraction of 48.35%. The lower fibre volume fraction associated with the original RVE lead to lower values of Young's and shear moduli as compared to one obtained in [25, 27, 45]. The associated mesh of the full RVE is also shown in Figure 3(b) consisting of 17,675 elements and 6,348 nodes. The geometry is meshed with tetrahedral elements and a periodic mesh consisting of exactly the same triangular mesh on opposite boundaries. Similarly,
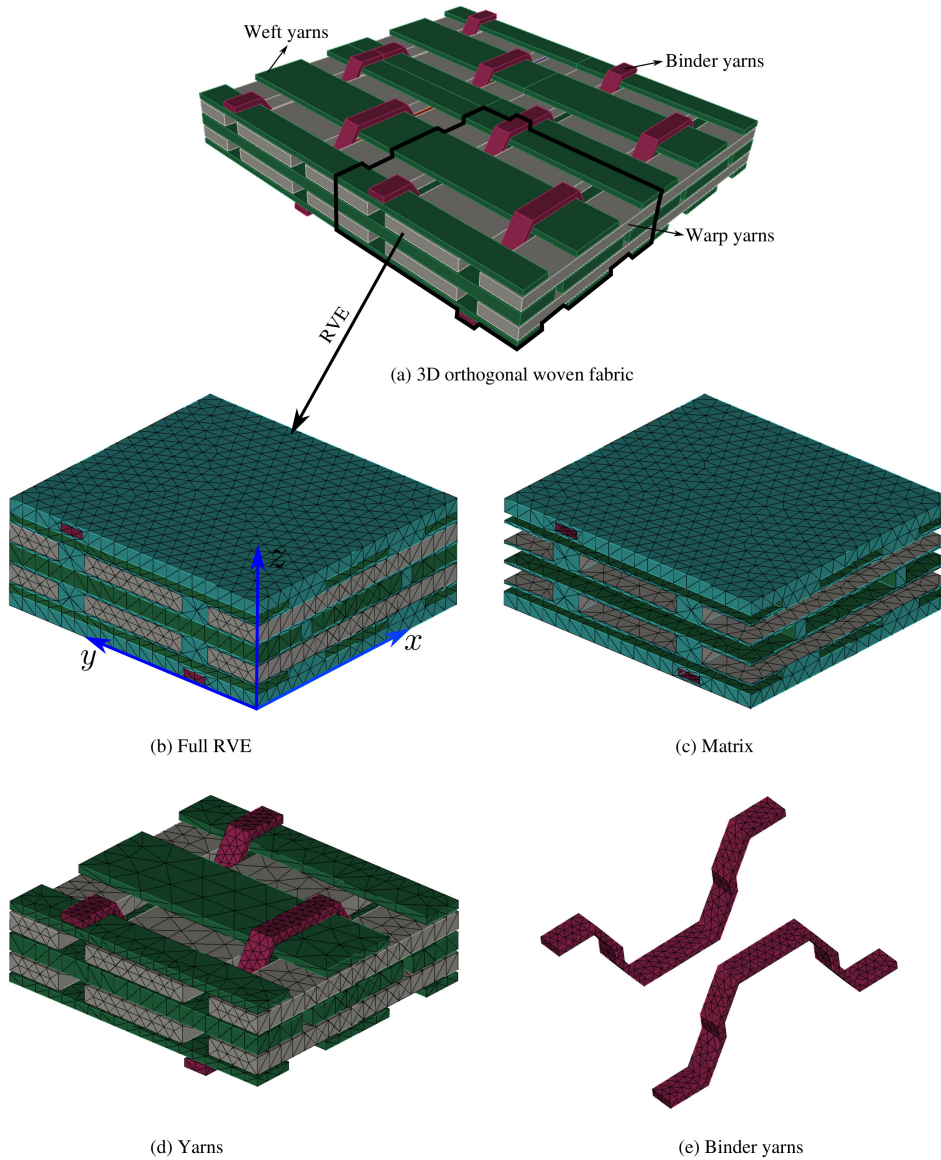
Figure 3: RVE of 3D orthogonal woven composite with straight edges.

meshes associated with matrix, yarns and binder yarns are shown in Figures 3(c), 3(d) and 3(e) respectively. The yarns mesh consists of 6,275 tetrahedral elements and 2,683 nodes and the matrix mesh consists of 11,400 tetrahedral elements and 3,665 nodes. Similarly for the modified RVE, the associated mesh consisting of 16,985 tetrahedral elements and 5,361 nodes and is shown in Figure 4(a). Moreover, meshes associated with yarns and binder yarns are shown in Figures 4(b) and 4(c) respectively. Only tetrahedral elements are used in this paper, generated using CUBIT. Tetrahedral elements are normally used for meshing complicated geometries with automatic (or semi-automatic) mesh generation algorithms [46]. Both tetrahedral and hexahedral meshes are used in [45] for the calculation of homogenised mechanical properties of 2×2 Twill woven composites. For the same number of elements, tetrahedral elements required a significantly lower number of degrees of freedom, leading to computational efficiency.

(a) Full RVE

(b) Yarns
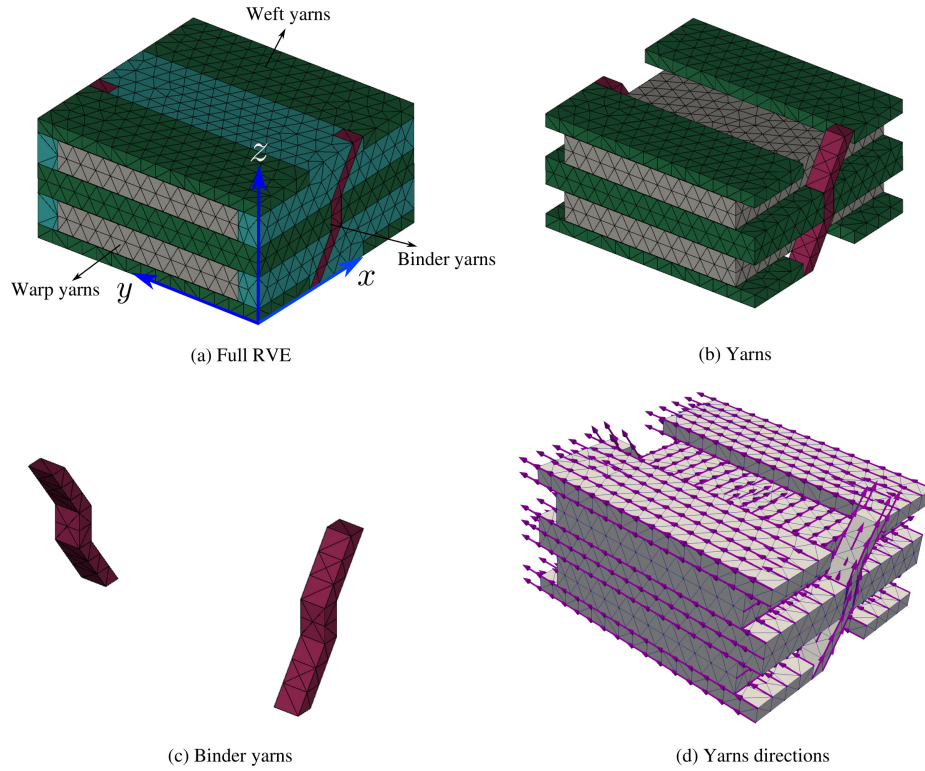
(c) Binder yarns

(d) Yarns directions

Figure 4: Modified RVE geometry and yarns direction for the 3D orthogonal woven composite with straight edges.

In [33], tetrahedral elements were used for the woven composites due to their complicated geometries. As described in §2.2, two and five material parameters are required for the matrix and yarns respectively. The material parameters for yarns and matrix are given in Tables 1 and 2 respectively. These material parameters are the same as those used in [25, 27, 45] for the S-2 glass fibre and Dow Derakane 8084 Vinyl Ester-Epoxy matrix materials.

Parameter	Value
E_p	14.66 GPa
E_z	53.12 GPa
ν_p	0.268
ν_{pz}	0.07341
G_{zp}	4.24 GPa

Table 1: Yarns material parameters for the 3D orthogonal woven composite with straight edges.

Parameter	Value
E	3.17 GPa
ν	0.35

Table 2: Matrix material parameters for the 3D orthogonal woven composite with straight edges.

The calculated yarns directions for the full and modified RVEs are shown in Figures 5 and

11

4(c) respectively. For the full RVE, the calculated nine homogenised material properties in the global coordinates x, y and z for the resulting orthotropic material are shown in Figures 6 and 7. In this case, three types of RVE boundary conditions including linear displacement, periodic and uniform traction are used to obtained these properties. These results are in accordance with §2.1, i.e. the linear displacement boundary condition generate the stiffest RVE response leading to higher values of Young's and shear moduli. On the other hand, the kinematically least constrained response of the uniform traction boundary condition leads to the lowest values of Young's and shear moduli. The effective properties calculated with the periodic boundary condition lie between the upper and lower limit of linear displacement and uniform traction boundary conditions [37, 47, 48]. A sample of the full deformed RVEs due to the application of $\overline{\varepsilon}_{xx} = 1$, subjected to linear displacement, periodic and uniform traction boundary conditions is shown in Figures 8(a), 8(b) and 8(c) respectively. Similarly, for the applied strain $\overline{\varepsilon}_{zz} = 1$ and $2\overline{\varepsilon}_{zx} = 1$, the deformed RVEs are given in Figures 9 and 10 respectively.

For the full RVE, these homogenised material properties are calculated using three order of approximations [38] as shown in Figures 6 and 7. These are represented by p_1, p_2 and p_3 in Figure 6(a). The associated degrees of freedom for p_1, p_2 and p_3 are 11,628 81,630 and 263,406 respectively. Homogenised material properties are changing from p_1 and p_2 but the change between p_2 and p_3 are negligibly small. Therefore, p_2 can be considered as the most appropriate order of approximation, given the high computational cost associated with p_3. The homogenised material properties in this case are also compared with results from [25, 27, 45], which are also plotted in Figures 6 and 7. Lower volume fraction of 31.0% in the case of a full RVE compared to 49.0% in [25, 27, 45] leads to lower values of Young and shear moduli. In addition to the stiffness contribution in the z direction as shown in Figure 6(c), binder yarns are also contributing to stiffness in the warp or x direction. Therefore, homogenised Young's modulus in the warp or x direction, i.e. $\overline{E}_{xx}$ as shown in Figure 6(a) is higher than the corresponding Young's modulus in the weft or y direction as shown in Figure 6(b). Similarly, the slightly higher values of out-of-plane shear modulus $\overline{G}_{xz}$ compared to $\overline{G}_{yz}$ which are shown in Figures 6(d) and 6(e) respectively are also due to the existence of binder yarns. The values of in-plane shear modulus $\overline{G}_{xy}$ as shown in Figure 6(f) are higher than both out-of-plane shear moduli, i.e. $\overline{G}_{xz}$ and $\overline{G}_{yz}$. The out-of-plane Poisson's ratios, i.e. $\overline{\nu}_{xz}$ and $\overline{\nu}_{yz}$ as shown in Figures 7(a) and 7(b) respectively are almost similar. The in-plane Poisson's ratio, i.e. $\overline{\nu}_{xy}$ as shown in Figure 7(c) is very small compared to both $\overline{\nu}_{xz}$ and $\overline{\nu}_{yz}$. This is due to the existence of warp and weft yarns in the x and y directions respectively restricting transverse deformation. For the modified RVE, a comparison between the homogenised material properties and the reference results from [25, 27, 45] is shown in Figures 11 and 12. A comparison between the full and modified RVE against the reference results are also given in Table 3. Compared to the full RVE, homogenised properties obtained with the modified RVE are in excellent agreement with the reference results. The excellent results obtained from the first numerical example provide us

with confidence to use the proposed computational framework for more complicated 3D-textile composites.
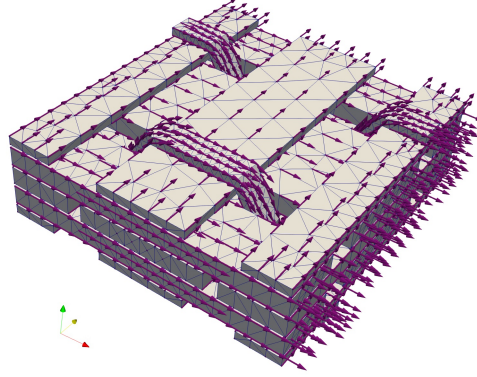

Figure 5: Yarn directions for the 3D orthogonal woven composite with straight edges.

Approach	$\overline{E}_{xx}$	$\overline{E}_{yy}$	$\overline{E}_{zz}$	$\overline{G}_{xy}$	$\overline{G}_{yz}$	$\overline{G}_{zx}$	$\overline{\nu}_{xy}$	$\overline{\nu}_{xz}$	$\overline{\nu}_{yz}$
Bogdanovich, 2006	27.31	25.7	9.98	3.58	3.58	3.34	0.125	0.432	0.448
Li, et.al., 2011	27.37	27.29	12.24	3.45	3.94	3.65	0.121	0.291	0.305
Bacarreza, et.al., 2012	28.68	27.4	12.31	3.52	3.9	3.77	0.12	0.305	0.295
Full RVE (displacement)	19.11	17.97	7.43	2.61	2.25	2.26	0.135	0.364	0.361
Full RVE (periodic)	19.03	17.92	7.24	2.55	2.07	2.07	0.133	0.368	0.368
Full RVE (traction)	14.39	14.31	6.85	2.46	2.05	2.06	0.151	0.380	0.375
Modified RVE (displacement)	28.30	26.78	11.83	3.53	3.74	3.81	0.122	0.303	0.302
Modified RVE (traction)	22.43	18.13	10.47	3.26	3.30	3.36	0.158	0.307	0.329

Table 3: Comparison of the homogenised mechanical properties of the full and modified RVEs against the values from literature

3.2. Comparative study of five different 3D-textile composites

In this example, a comparative study is performed to investigate the homogenised mechanical properties of the following five 3D-textile composites consisting of 2.5D and 3D yarns architectures.

- 3D-textile composites with 3D yarn architecture

    - 3D orthogonal interlock (3D-OI),

    - 3D layer-to-layer interlock (3D-LTLI),

    - 3D through-the-thickness angle interlock (3D-TTTAI),

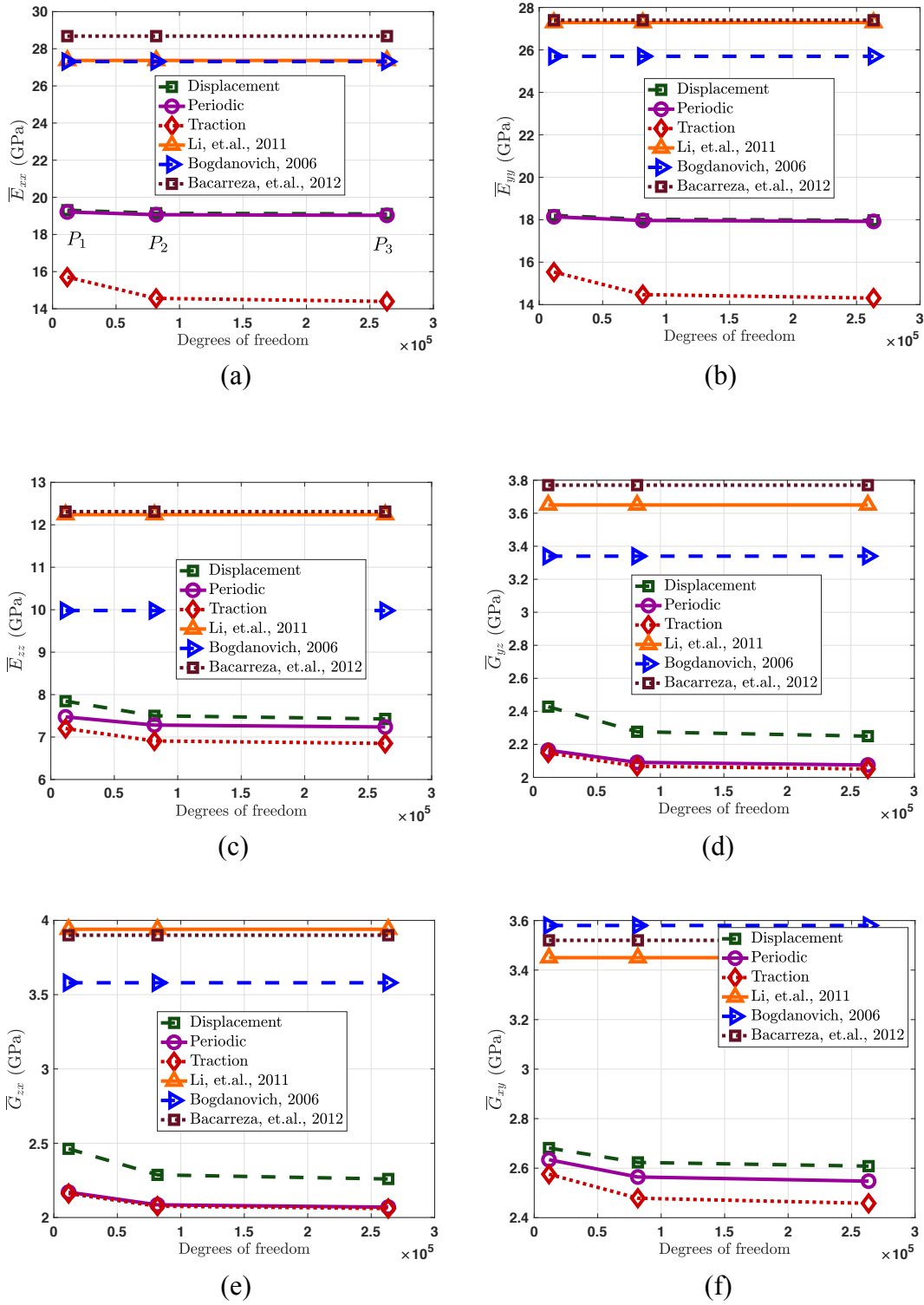- 3D-textile composites with 2.5D yarn architecture

Figure 6: Homogenised Young's and shear moduli for the 3D orthogonal woven composite with straight edges.

- 2.5D layer-to-layer angle interlock (2.5D-LTLAI),

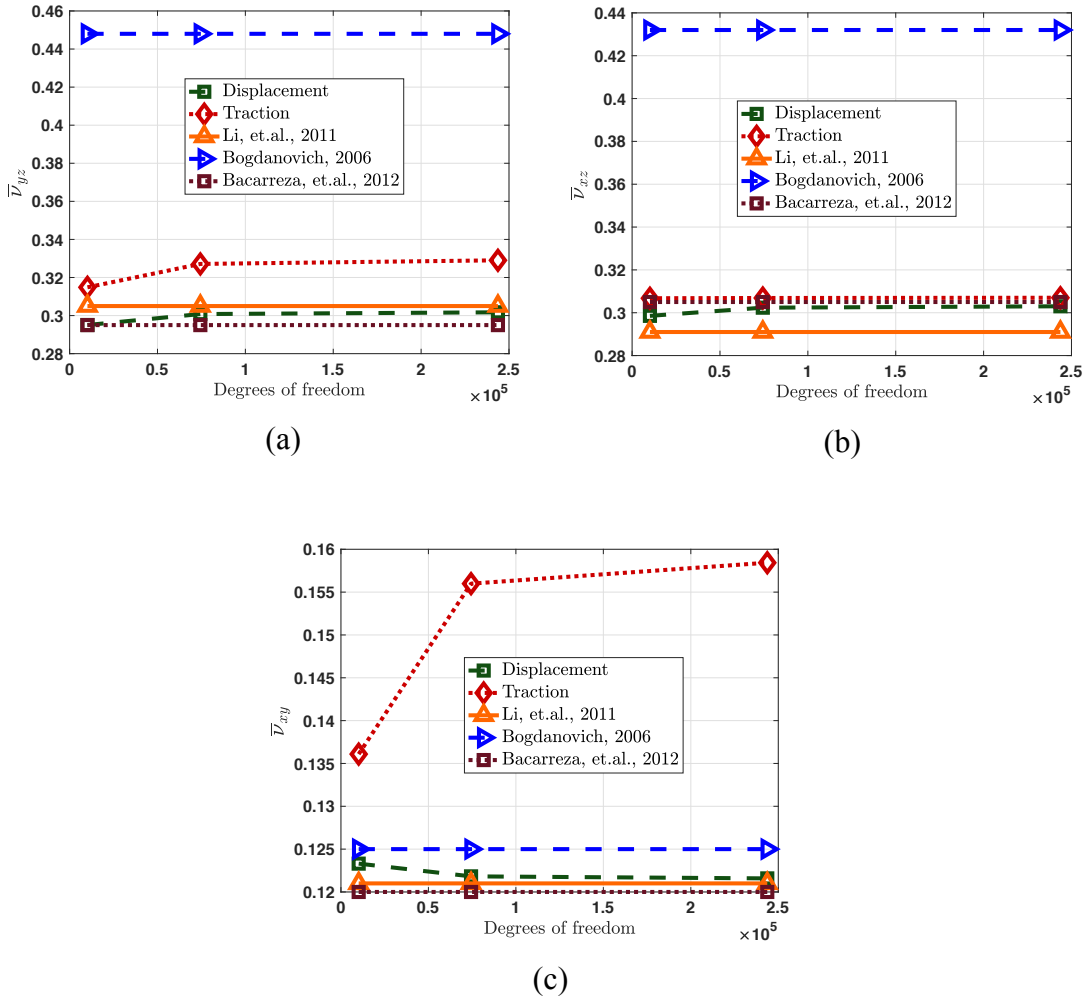- 2.5D layer-layer angle interlock or through-the-thickness angle interlock (2.5D-LLAI),

Figure 7: Homogenised Poisson's ratios for the 3D orthogonal woven composite with straight edges.
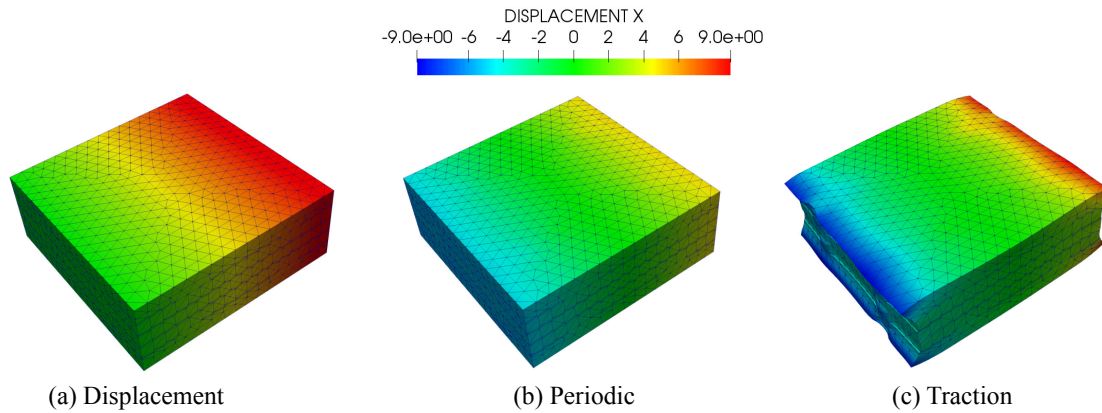

(a) Displacement   (b) Periodic   (c) Traction

Figure 8: Deformed RVE due to applied strain $\overline{\varepsilon}_{xx} = 1$ for the 3D orthogonal woven composite with straight edges.

The full details of their geometrical description are given in [8]. Yarns geometry are modelled with elliptical cross-sections and cubic spline paths. For the composites with 3D-textile yarns
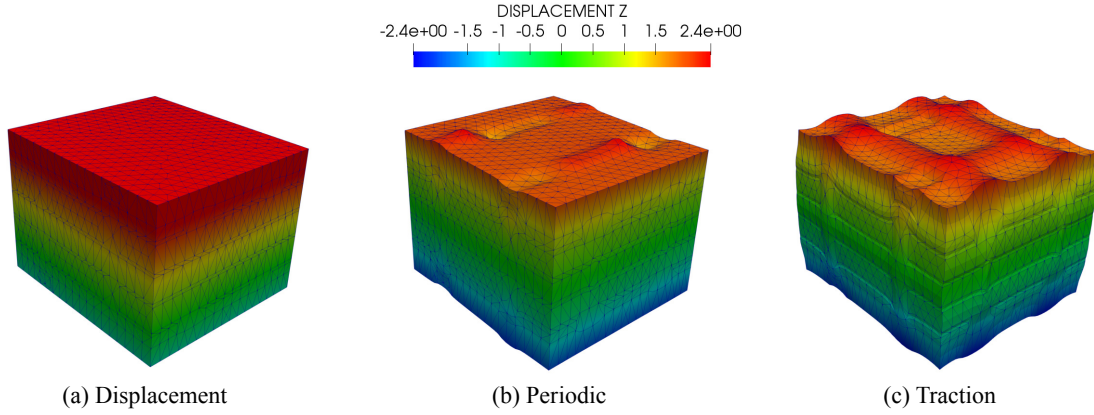
Figure 9: Deformed RVE due to applied strain $\overline{\varepsilon}_{zz} = 1$ for the 3D orthogonal woven composite with straight edges.
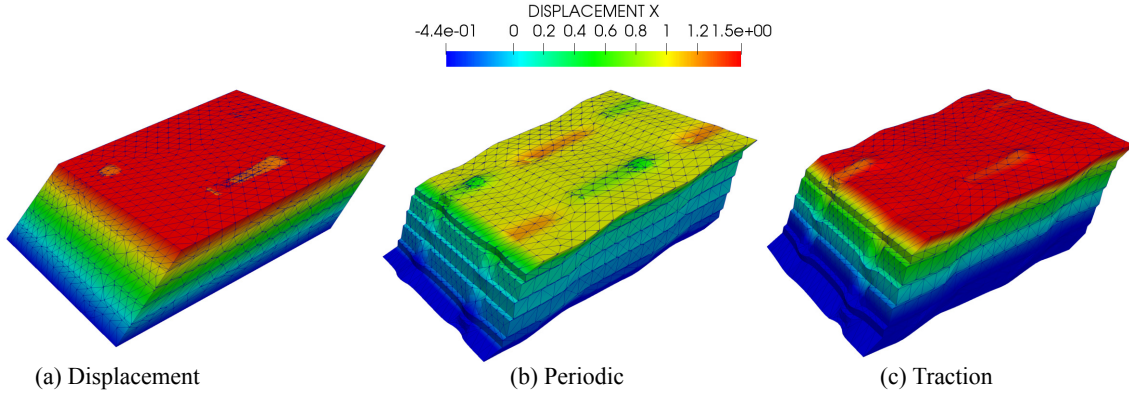

Figure 10: Deformed RVE due to applied strain $2\overline{\varepsilon}_{zx} = 1$ for the 3D orthogonal woven composite with straight edges.

architectures, the dimensions of weft, warp and binder yarns are given in Table 4. Spacing between weft (L_f), warp (L_p) and binder (L_b) yarns are also given in the same table. For the composites with 2.5D yarns architectures the corresponding dimensions are given in Table 5. For the 3D-OI, the geometry with mesh and coordinate system is shown in 13(a) consisting of two layers of warp yarns and three layers of weft yarns. Only yarns and corresponding front view are also shown in Figures 13(b) and 13(c) respectively. A very similar geometrical description for 3D-LTLI, 3D-TTTAI, 2.5D-LTLAI and 2.5D-LLAI RVEs is given in Figures 14, 15, 16 and 17 respectively. The dimensions of the RVEs in x, y and z directions and their corresponding volumes are given in Table 6. The volume fraction of matrix ($Vm = v_m/v_{RVE}$), warp yarns ($Vp = v_p/v_{RVE}$), weft yarns ($Vf = v_f/v_{RVE}$) and binder yarns ($Vb = v_b/v_{RVE}$), are calculated using CUBIT/Trelis and are given in Table 7. Here v_m, v_p, v_f, v_b, v_{RVE} are volumes of matrix, warp yarns, weft yarns, binder yarns and full RVE respectively. The material properties for yarns and matrix used in this case are similar to those used in the previous example and are given in Tables 1 and 2 respectively.
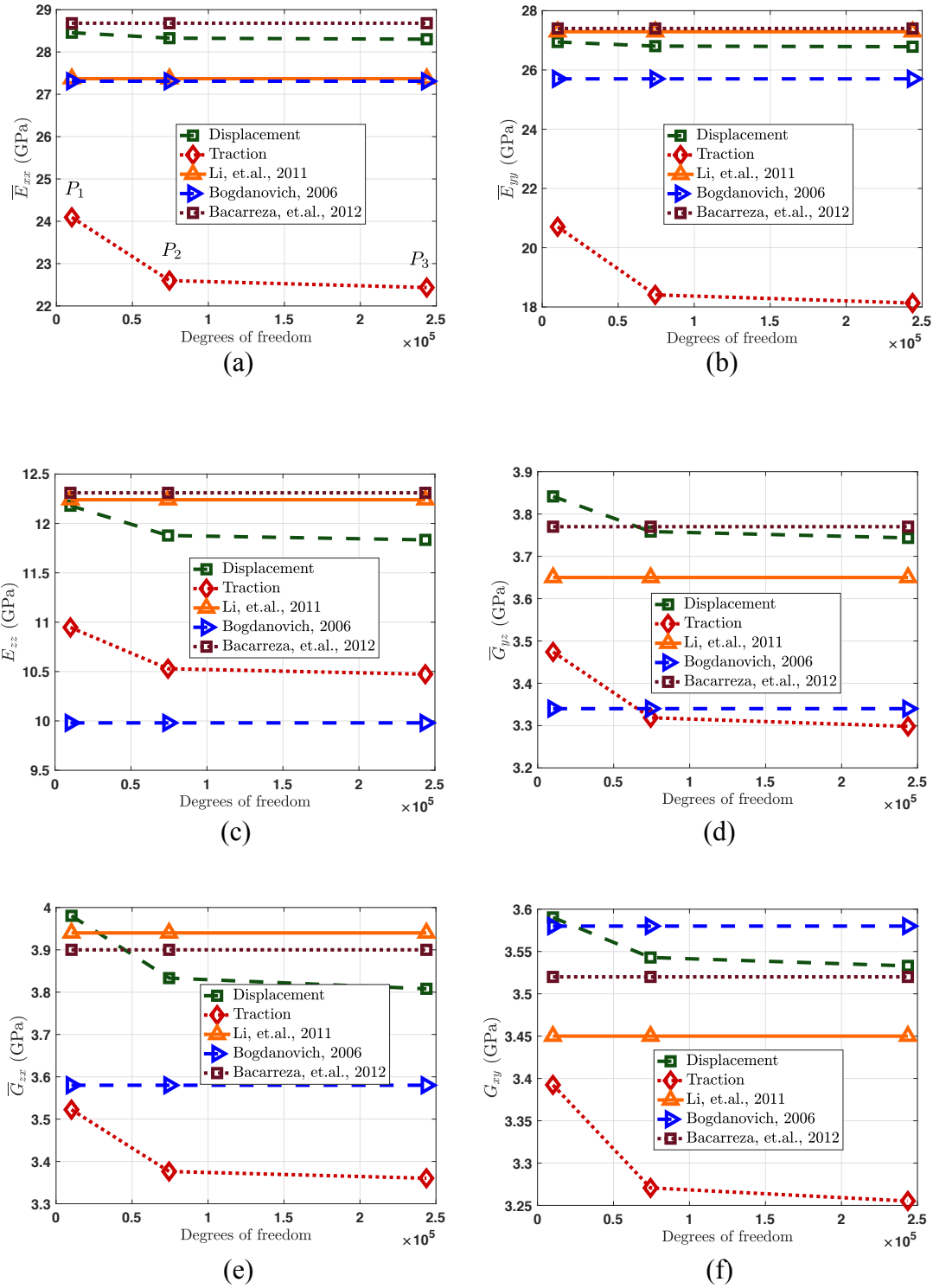
16

Figure 11: Homogenised Young's and shear moduli using modified RVE for the 3D orthogonal woven composite with straight edges.

The proposed computational framework is used to calculate the homogenised mechanical properties of these five composites. Similarly to the previous example, three orders of approximation
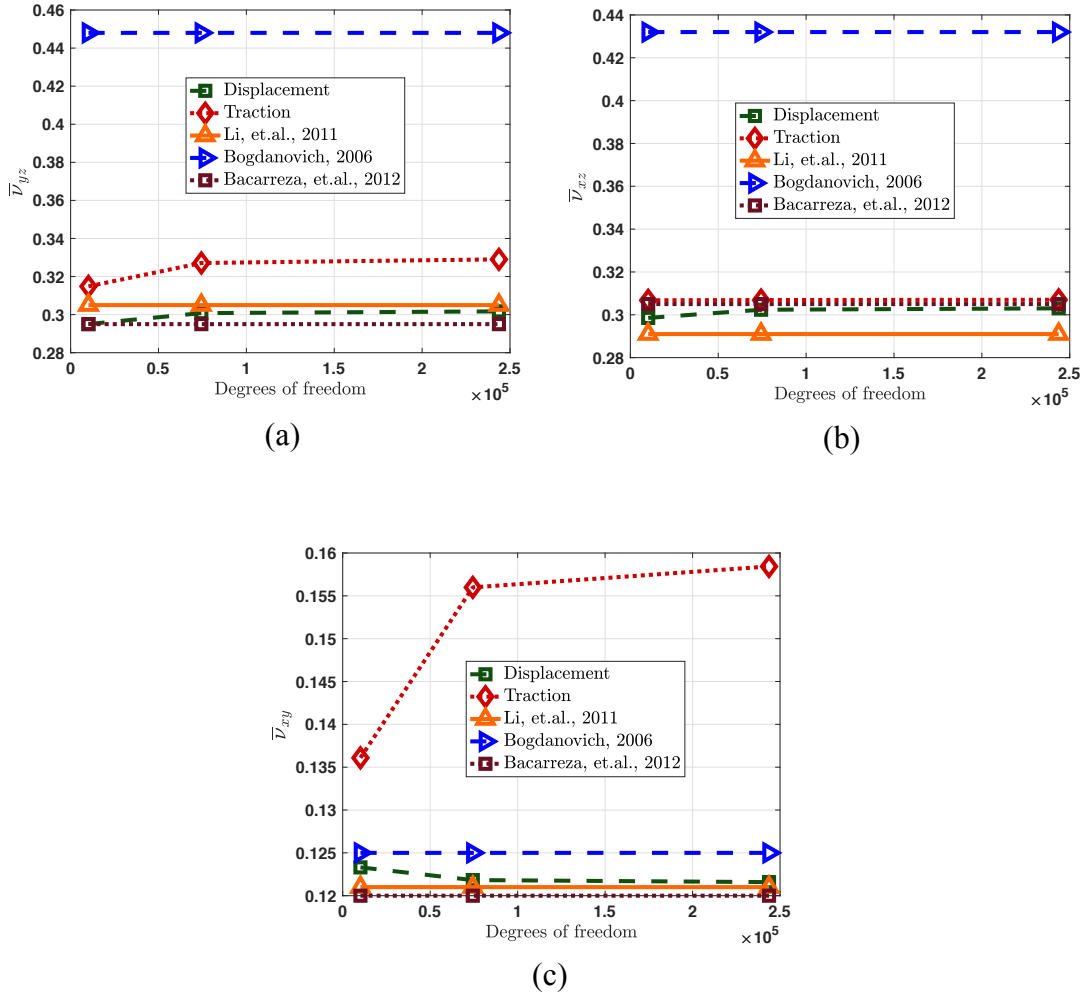
Figure 12: Homogenised Poisson's ratios using modified RVE for the 3D orthogonal woven composite with straight edges.

are used. The number of elements and the corresponding degrees of freedom for the first ($p = 1$), second ($p = 2$) and third ($p = 3$) order of a approximation are given in Table 8. The resultant yarns directions determined using potential flow theory (§2.2) are shown in Figures 18(a), 18(b), 18(c), 18(d), 18(e) for 3D-OI, 3D-LTLI, 3D-TTTAI, 2.5D-LTLAI and 2.5D-LLAI respectively. In this example, only the liner displacement boundary conditions is used to impose the RVE boundary conditions. A comparison of the homogenised mechanical properties of the five 3D-textile composites are shown in Figures 19 and 20. As in the previous example, the homogenised mechanical properties decrease from p_1 to p_2 but the difference between p_2 to p_3 are negligible. A comparison for $\overline{E}_{xx}$ including five different composites and three orders of approximation are given in 19(a). For a composite with 3D yarns architectures, the values of $\overline{E}_{xx}$ is very high as compared to one with 2.5D yarns architectures. This may be due to very high V_p for composites with 3D yarns architectures ($V_p \geq 13.39\%$) as compared to one with 2.5D yarns architectures ($V_p = 7.60\%$). For all three composites with 3D yarns architectures,

18

values of $\overline{E}_{xx}$ are almost similar but the 3D-TTTAI has the highest values followed by 3D-LTLI while 3D-OI has the lowest values. For the two composites with 2.5D yarns architectures, LLAI has higher values of $\overline{E}_{xx}$ as compared to LTLAI. It is clear from Figure 19(a) that multiple factors can affect values of $\overline{E}_{xx}$ including yarns architectures and volume fraction of warp (V_p) and binder (V_b) yarns.

A comparison of the homogenised Young's modulus in the y direction, i.e. $\overline{E}_{yy}$, is given in Figure 19(b). For all five composites, the large sizes and corresponding large V_f of weft yarns leads to higher values of $\overline{E}_{yy}$ as compared to the corresponding values of $\overline{E}_{xx}$. Similar to $\overline{E}_{xx}$, values of $\overline{E}_{yy}$ are higher for composites with 3D yarns architecture as compared to one with 2.5D yarns architecture. A very similar architecture of the weft yarns and corresponding equal values of V_f for the three composites with 3D yarns architectures lead to very similar values of $\overline{E}_{yy}$. The slightly lower values of E_y for 3D-TTTAI may be due to a lower $V_f = 23.73\%$ as compared to $V_f = 23.92\%$ for both 3D-OI and 3D-LTLI. Similarly, the two composites with 2.5D yarns architectures have very similar values of E_y, which is again due to their similar yarns architectures in the weft direction and corresponding similar values of V_f. The slightly higher values for 2.5D-LTLAI may be due to the higher value of $V_f = 14.11\%$ as compared to $V_f = 12.33\%$ for 2.5D-LLAI. A comparison of through-the-thickness Young's modulus ($\overline{E}_{zz}$) for all five composites is shown in Figure 19(c). As with $\overline{E}_{xx}$ and $\overline{E}_{yy}$, values of $\overline{E}_{zz}$ are higher for composites with 3D yarns architectures as compared those with 2.5D yarns architectures. For the composites with 3D yarn architecture, 3D-OI has the highest $\overline{E}_{zz}$ followed by 3D-LTLI while 3D-TTTAI has the lowest values. For the composites with 2.5D yarn architecture, 2.5D-LTLAI has higher value of E_z as compared to 2.5D-LLAI. For all three shear moduli $\overline{G}_{xy}$, $\overline{G}_{yz}$ and $\overline{G}_{zx}$, a consistent trend can be seen in Figures 19(d), 19(e) and 19(f) respectively for both composites with 3D and 2.5D yarns architectures. For the composites with 3D yarns architectures, 3D-LTLI has the highest values of shear moduli followed by 3D-OI while 3D-TTTAI has the lowest values. For composites with 2.5D yarns architecture, 2.5D-LTLAI has higher values of shear moduli as compared to 2.5D-LLAI. Finally, a comparison of the homogenised Poisson's ratios $\overline{\nu}_{xy}$, $\overline{\nu}_{xz}$ and $\overline{\nu}_{yz}$ for the five composites is shown in Figures 20(a), 20(b) and 20(c) respectively. As with the previous example, in-plane Poisson's ratio $\overline{\nu}_{xy}$ are very small compared to the out-of-plane Poisson's ratio $\overline{\nu}_{xz}$ and $\overline{\nu}_{yz}$.

Yarns	Width (mm)	Thickness (mm)	Spacing
Weft	0.27	0.15	$L_f = 0.429$
Warp	0.25	0.15	$L_p = 0.473$
Binder	0.08	0.05	$L_b = 0.473$

Table 4: Geometry parameters for composites with 3D yarns architecture.

Yarns	Width (mm)	Thickness (mm)	Spacing
Weft	0.25	0.15	$L_f = 1.0$
Warp	0.25	0.15	$L_p = 0.5$

Table 5: Geometry parameters for composites with 2.5D yarns architectures.

	3D-OI	3D-LTLI	3D-TTTAI	2.5D-LTLAI	2.5D-LLAI
L_x (mm)	0.858	0.858	2.145	2.000	4.000
L_y (mm)	0.946	0.946	2.365	1.000	2.000
L_z (mm)	0.930	0.930	1.250	1.550	1.550
Volume (mm^3)	0.755	0.755	6.341	3.100	12.400

Table 6: RVEs sizes and volume for composites with 2.5D and 3D yarns architectures.

Composite	Volume RVE	V_m %	V_P %	V_f %	V_b %
3D-OI	0.75	60.82	13.39	23.92	1.87
3D-LTLI	0.75	60.24	13.39	23.92	2.45
3D-TTTAI	6.34	60.57	14.94	23.73	0.76
2.5D-LTLAI	3.10	78.29	7.60	14.11	0.00
2.5D-LLAI	12.40	80.07	7.60	12.33	0.00

Table 7: Volume fraction of yarns and matrix for composites with 2.5D and 3D yarns architectures.

Composite	Elements	DOFs (1st order)	DOFs 2nd order	DOFs 3rd order
3D-OI	23, 110	12, 957	97, 626	323, 340
3D-LTLI	45, 915	25, 002	190, 656	634, 710
3D-TTTAI	86, 734	46, 671	362, 439	1, 209, 000
2.5D-LTLAI	16, 192	9, 711	71, 355	233, 511
2.5D-LLAI	42, 423	23, 358	179, 070	594, 408

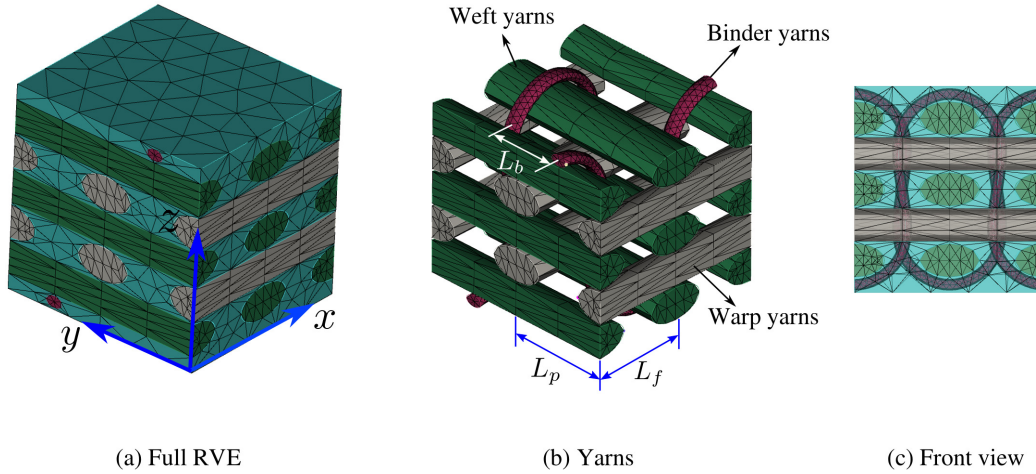Table 8: Number of elements and degrees of freedom for composites with 2.5D and 3D yarns architectures.

(a) Full RVE　　　　　　　(b) Yarns　　　　　　　(c) Front view

Figure 13: Representative volume element for 3D orthogonal interlock.

(a) Full RVE   (b) Yarns   (c) Front view
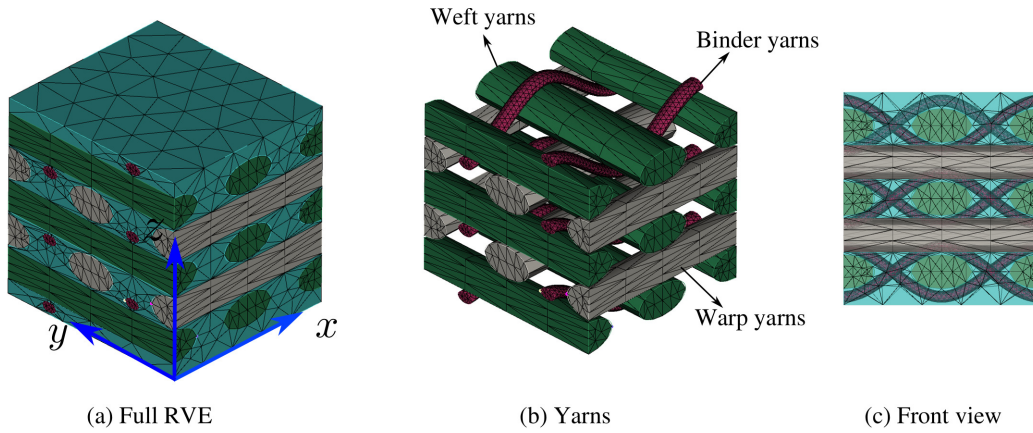
Figure 14: Representative volume element for 3D layer-to-layer interlock.

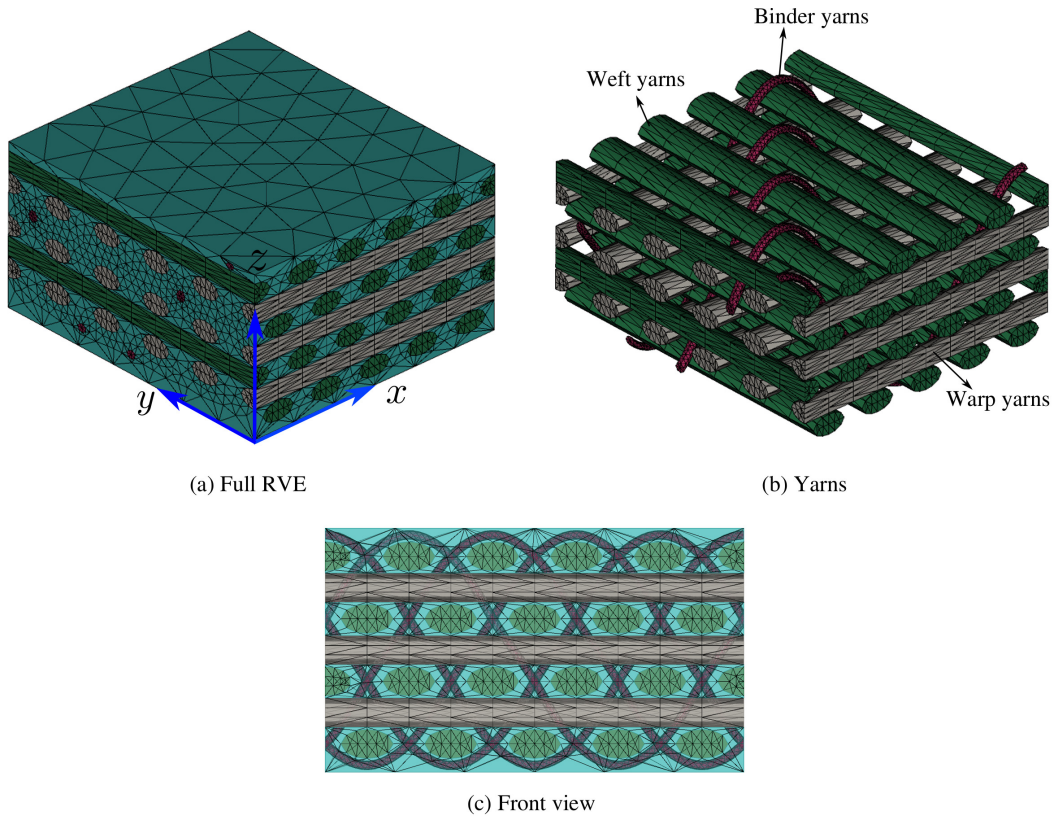(a) Full RVE   (b) Yarns

(c) Front view

Figure 15: Representative volume element for 3D through-the-thickness angle interlock.

4. Concluding remarks

A novel, multi-scale, computational framework is proposed for the calculation of the homogenised mechanical properties of 3D textile/woven FRP composites. In addition to the unified approach used for the imposition of the RVE boundary conditions, the computational framework has additional flexibility of hierarchic basis functions and high-performance computing. Matrix and yarns are modelled as isotropic and transversely isotropic materials. A very
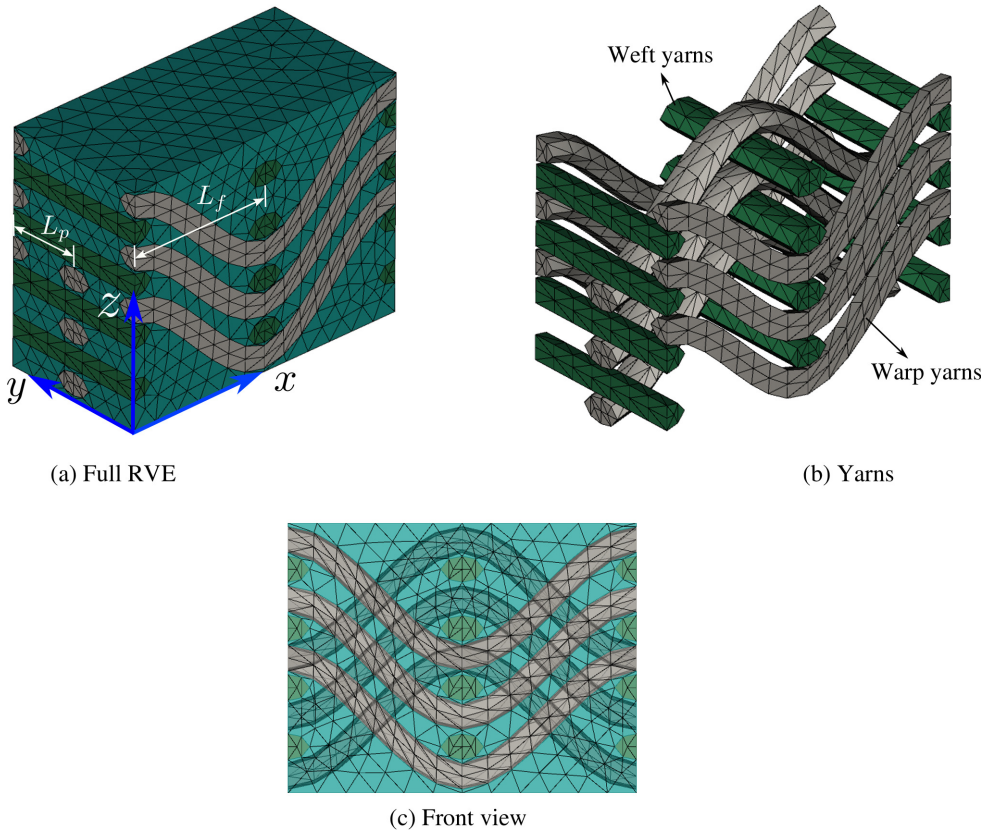
(a) Full RVE

(b) Yarns

(c) Front view

Figure 16: Representative volume element for 2.5D layer-to-layer angle interlock.

generalised and robust procedure based on the potential flow theory is used for the calculation of the yarns' principle directions, required for the transversely isotropic material model. Yarns geometry are modelled with elliptical cross-sections and cubic spline paths. The computational framework is implemented within an open-source finite element code MOFEM (Mesh-Oriented Finite Element Method). Two numerical examples are presented to demonstrate the implementation and performance of the developed computational framework.The first numerical example is a 3D orthogonal woven composite with oversimplified yarns geometry consisting of rectangular cross-section. Two different RVEs geometries are considered for the first numerical example. The original RVE geometry has a lower fibre volume fraction of 31.0% while the modified geometry has a fibre volume fraction of 48.35%. The calculated homogenised mechanical properties for both original and modified RVEs are compared with the results from literature. As compared to the full RVE, homogenised properties obtained with the modified RVE are in excellent agreement with the reference results. In the second numerical example, a detailed comparison is made between the homogenised mechanical properties of 3D-textile composites with 3D and 2.5D yarns architectures. It was shown that multiple factors including yarns architecture and volume fraction contribute toward the homogenised mechanical properties and therefore required a detailed computational modelling. Although, the proposed computational framework, is used for the calculation of the homogenised mechanical properties of 3D-textile

(a) Full RVE
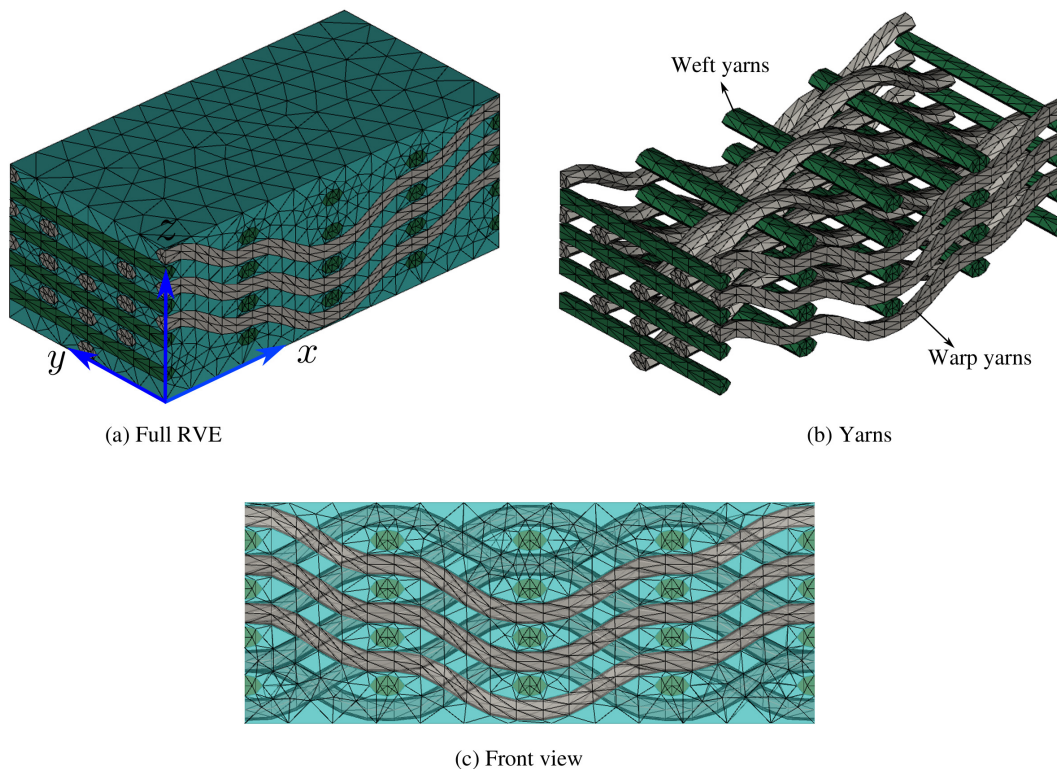
(b) Yarns

(c) Front view

Figure 17: Representative volume element for 2.5D layer-layer angle interlock.

composites in this paper it is equally applicable to other composites with unidirectional and 2D-textile reinforcements. Moreover, in addition to the calculation of homogenised mechanical properties, the proposed computational framework can also be used for the calculation of the homogenised thermal and moisture transport properties.

Acknowledgements

Appendix A. Relationship between mathematical and engineering constants

At macro/structural-level, 3D textile composites can be considered as homogeneous and orthotropic material. Relation between stress and strain for an orthotropic material model is
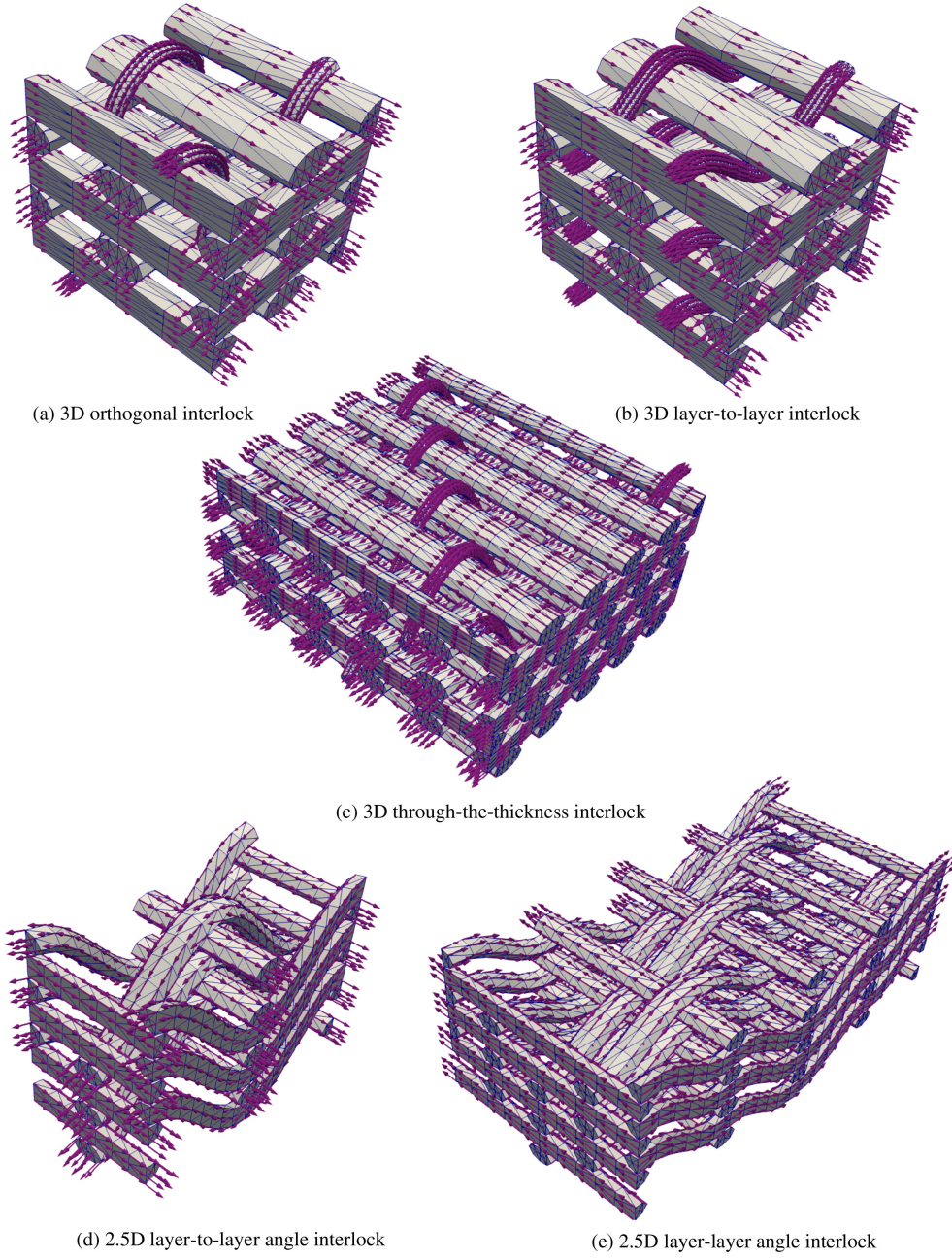
(a) 3D orthogonal interlock

(b) 3D layer-to-layer interlock

(c) 3D through-the-thickness interlock

(d) 2.5D layer-to-layer angle interlock

(e) 2.5D layer-layer angle interlock

Figure 18: Directions of fibres in the yarns for composites with 2.5D and 3D yarns architecture.

written as

$$
\left\{
\begin{array}{c}
\overline{\varepsilon}_{xx} \\
\overline{\varepsilon}_{yy} \\
\overline{\varepsilon}_{zz} \\
\overline{\gamma}_{xy} \\
\overline{\gamma}_{yz} \\
\overline{\gamma}_{zx}
\end{array}
\right\}
= \overline{\mathbf{S}}
\left\{
\begin{array}{c}
\overline{\sigma}_{xx} \\
\overline{\sigma}_{yy} \\
\overline{\sigma}_{zz} \\
\overline{\tau}_{xy} \\
\overline{\tau}_{yz} \\
\overline{\tau}_{zx}
\end{array}
\right\},
\qquad \text{where} \qquad
\overline{\mathbf{S}} = \overline{\mathbf{C}}^{-1},
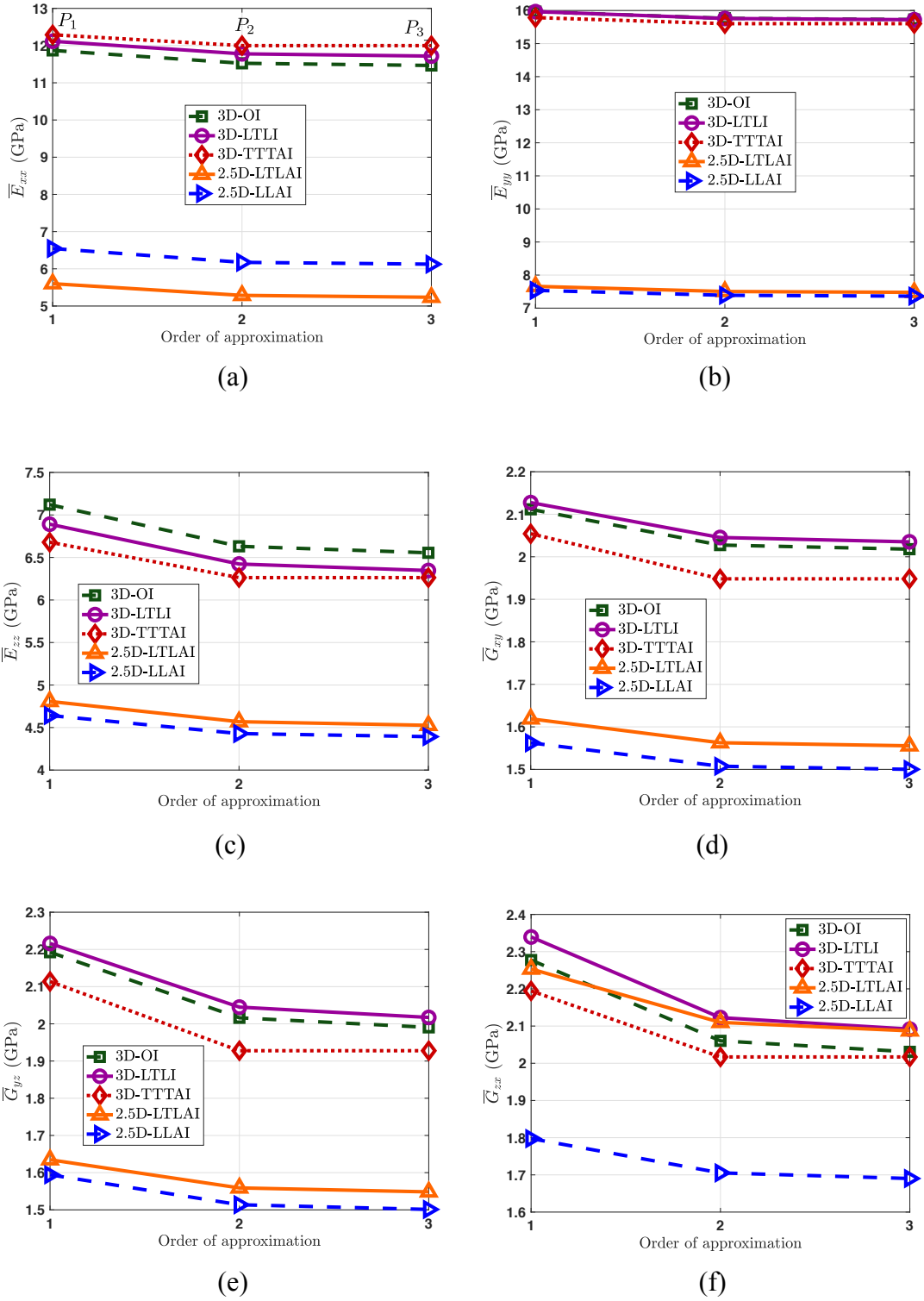\tag{A.1}
$$

Figure 19: Homogenised Young's and shear moduli for composites with 2.5D and 3D yarns architecture.

here $\overline{\mathbf{C}}$ and $\overline{\mathbf{S}}$ are homogenised stiffness and compliance matrices respectively. For an orthotropic material model, compliance matrix $\overline{\mathbf{S}}$ is written as
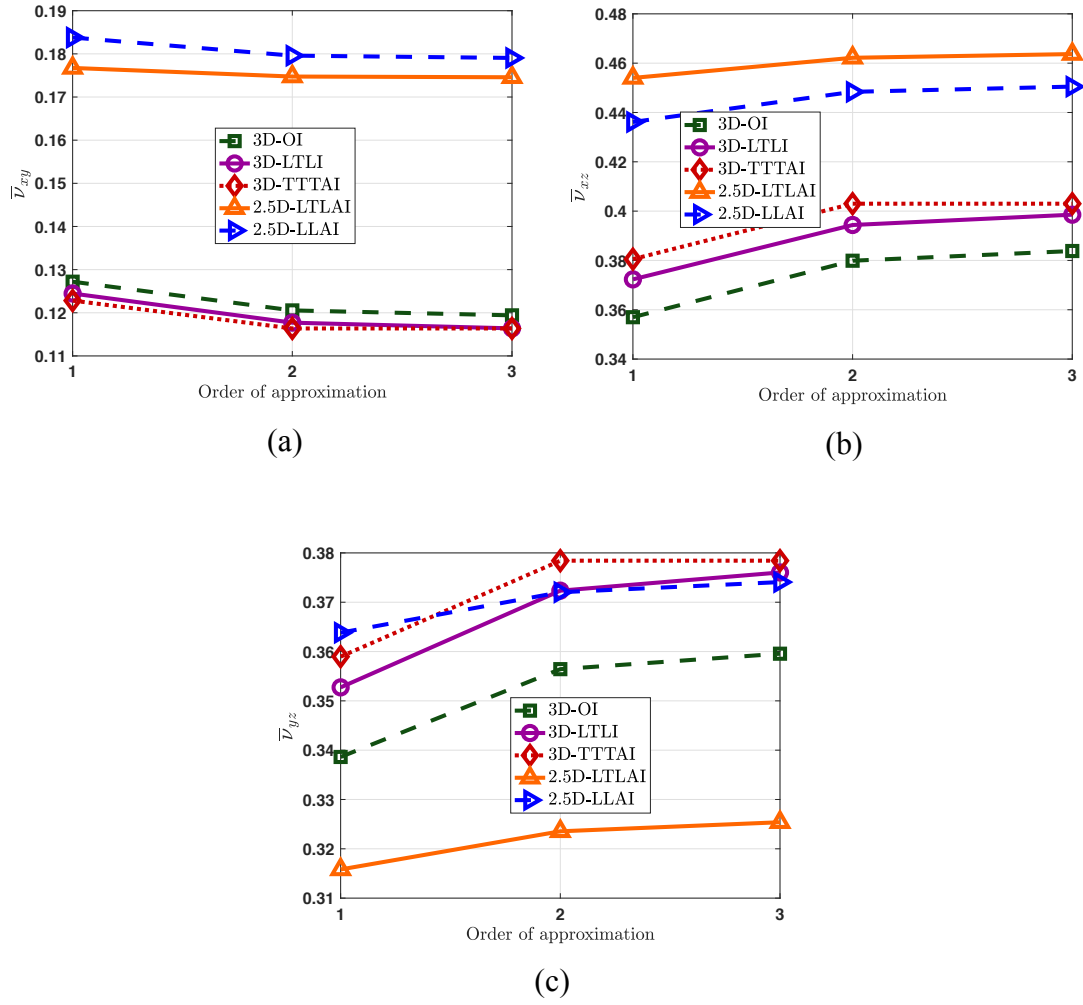
(a)

(b)

(c)

Figure 20: Homogenised Poisson's ratios for composites with 2.5D and 3D yarns architecture.

$$\overline{\mathbf{S}} = \begin{bmatrix} \dfrac{1}{\overline{E}_{xx}} & -\dfrac{\overline{\nu}_{yx}}{\overline{E}_{yy}} & -\dfrac{\overline{\nu}_{zx}}{\overline{E}_{zz}} & 0 & 0 & 0 \\[2mm] -\dfrac{\overline{\nu}_{xy}}{\overline{E}_{xx}} & \dfrac{1}{\overline{E}_{yy}} & -\dfrac{\overline{\nu}_{zy}}{\overline{E}_{zz}} & 0 & 0 & 0 \\[2mm] -\dfrac{\overline{\nu}_{xz}}{\overline{E}_{xx}} & -\dfrac{\overline{\nu}_{yz}}{\overline{E}_{yy}} & \dfrac{1}{\overline{E}_{zz}} & 0 & 0 & 0 \\[2mm] 0 & 0 & 0 & \dfrac{1}{\overline{G}_{xy}} & 0 & 0 \\[2mm] 0 & 0 & 0 & 0 & \dfrac{1}{\overline{G}_{yz}} & 0 \\[2mm] 0 & 0 & 0 & 0 & 0 & \dfrac{1}{\overline{G}_{zx}} \end{bmatrix}, \tag{A.2}$$

where x, y and z are global coordinate axes associated with the 3D textile composites RVE. With calculated homogenised stiffness matrix $\overline{\mathbf{C}}$, the three homogenised Young's moduli are calculated as

$$\overline{E}_{xx} = \frac{1}{\overline{S}_{11}}, \qquad \overline{E}_{yy} = \frac{1}{\overline{S}_{22}} \qquad \text{and} \quad \overline{E}_{zz} = \frac{1}{\overline{S}_{33}}. \tag{A.3}$$

26

Similarly, the three homogenised shear moduli are written as

$$\overline{G}_{xy} = \frac{1}{\overline{S}_{44}}, \qquad \overline{G}_{yz} = \frac{1}{\overline{S}_{55}} \qquad \text{and} \quad \overline{G}_{zx} = \frac{1}{\overline{S}_{66}}, \tag{A.4}$$

and, the three homogenised Poisson's ratios are written as

$$\overline{\nu}_{xy} = -\overline{S}_{21}\overline{E}_{xx}, \qquad \overline{\nu}_{xz} = -\overline{S}_{31}\overline{E}_{xx} \qquad \text{and} \quad \overline{\nu}_{yz} = -\overline{S}_{32}\overline{E}_{yy} \tag{A.5}$$

Finally, the symmetry of the compliance matrix $\overline{\mathbf{S}}$ can be used to calculate Poisson's ratios $\overline{\nu}_{yx}$, $\overline{\nu}_{zx}$ and $\overline{\nu}_{zy}$, i.e.

$$\frac{\nu_{yx}}{E_{yy}} = \frac{\nu_{xy}}{E_{xx}}, \qquad \frac{\nu_{zx}}{E_{zz}} = \frac{\nu_{xz}}{E_{xx}} \qquad \text{and} \quad \frac{\nu_{zy}}{E_{zz}} = \frac{\nu_{yz}}{E_{yy}} \tag{A.6}$$

References

[1] L. Tong, A. P. Mouritz, M. K. Bannister, 3D Fibre Reinforced Polymer Composites, Elsevier Science, Oxford, 2002.

[2] A. Mouritz, M. Bannister, P. Falzon, K. Leong, Review of applications for advanced three-dimensional fibre textile composites, Composites Part A: Applied Science and Manufacturing 30 (12) (1999) 1445 – 1461.

[3] A. C. Long (Ed.), Design and manufacture of textile composites, Woodhead Publishing Series in Textiles, Cambridge England, 2005.

[4] X. Tang, J. D. Whitcomb, Y. Li, H.-J. Sue, Micromechanics modeling of moisture diffusion in woven composites, Composites Science and Technology 65 (6) (2005) 817 – 826.

[5] S. Buchanan, A. Grigorash, E. Archer, A. McIlhagger, J. Quinn, G. Stewart, Analytical elastic stiffness model for 3D woven orthogonal interlock composites, Composites Science and Technology 70 (11) (2010) 1597 – 1604.

[6] A. Hallal, R. Younes, F. Fardoun, S. Nehme, Improved analytical model to predict the effective elastic properties of 2.5D interlock woven fabrics composite, Composite Structures 94 (10) (2012) 3009 – 3028.

[7] K. C. Warren, R. A. Lopez-Anido, J. Goering, Experimental investigation of three-dimensional woven composites, Composites Part A: Applied Science and Manufacturing 73 (2015) 242 – 259.

[8] Y. Rahali, M. Assidi, I. Goda, A. Zghal, J. Ganghoffer, Computation of the effective mechanical properties including nonclassical moduli of 2.5D and 3D interlocks by microme-

chanical approaches, Composites Part B: Engineering 98 (Supplement C) (2016) 194 – 212.

[9] B. Sun, B. Gu, X. Ding, Compressive behavior of 3-D angle-interlock woven fabric composites at various strain rates, Polymer Testing 24 (4) (2005) 447 – 454.

[10] J. Brandt, K. Drechsler, F.-J. Arendts, Mechanical performance of composites based on various three-dimensional woven-fibre preforms, Composites Science and Technology 56 (3) (1996) 381 – 386.

[11] D. Jetavat, Near net shape preforming by 3D weaving process, Ph.D. thesis, Textile Composites Group, School of Materials, The University of Manchester (2012).

[12] S. Rudov-Clark, A. Mouritz, L. Lee, M. Bannister, Fibre damage in the manufacture of advanced three-dimensional woven composites, Composites Part A: Applied Science and Manufacturing 34 (10) (2003) 963 – 970.

[13] L. Lee, S. Rudov-Clark, A. Mouritz, M. Bannister, I. Herszberg, Effect of weaving damage on the tensile properties of three-dimensional woven composites, Composite Structures 57 (1) (2002) 405 – 413.

[14] M. Ansar, W. Xinwei, Z. Chouwei, Modeling strategies of 3D woven composites: A review, Composite Structures 93 (8) (2011) 1947 – 1963.

[15] F. Stig, 3D-woven reinforcement in composites, Ph.D. thesis, KTH School of Engineering Sciences, Sweden (2012).

[16] S. Hallstrom, 3D-textile reinforcement in composites- mechanics, modelling, pros and cons, in: 15th European Conference on Composite Materials, Venice, Italy, 24-28 June 2012.

[17] Z. Ullah, Ł. Kaczmarczyk, S. Grammatikos, M. Evernden, C. Pearce, Multi-scale computational homogenisation to predict the long-term durability of composite structures, Computers & Structures 181 (2017) 21 – 31.

[18] Z. Ullah, L. Kaczmarczyk, C. Pearce, Three-dimensional nonlinear micro/meso-mechanical response of the fibre-reinforced polymer composites, Composite Structures 161 (2017) 204 – 214.

[19] B. V. Sankar, R. V. Marrey, Analytical method for micromechanics of textile composites, Composites Science and Technology 57 (6) (1997) 703 – 713.

[20] J.-M. Yang, C.-L. Ma, T.-W. Chou, Fiber inclination model of three-dimensional textile structural composites, Journal of Composite Materials 20 (5) (1986) 472–484.

[21] R. A. Nalk, Analysis of woven and braided fabric reinforced composites., Tech. Rep. NASA CR-194930, National Aeronautics and Space Administration, Washington, DC (1994).

[22] B. N. Cox, F. Gerry, Handbook of analytical methods for textile composites. hampton, Tech. Rep. NASA Contractor Report 4750, National Aeronautics and Space Administration, Langley Research Center (1997).

[23] A. Hallal, R. Younes, F. Fardoun, Review and comparative study of analytical modeling for the elastic properties of textile composites, Composites Part B: Engineering 50 (0) (2013) 22 – 31.

[24] A. Kalamkarov, E. Hassan, A. Georgiades, M. Savi, Asymptotic homogenization model for 3D grid-reinforced composite structures with generally orthotropic reinforcements, Composite Structures 89 (2) (2009) 186 – 196.

[25] A. E. Bogdanovich, Multi-scale modeling, stress and failure analyses of 3-D woven composites, Journal of Materials Science 41 (20) (2006) 6547–6590.

[26] M. Rao, B. Sankar, G. Subhash, Effect of Z-yarns on the stiffness and strength of three-dimensional woven composites, Composites Part B: Engineering 40 (6) (2009) 540 – 551.

[27] L. Li, P. Wen, M. Aliabadi, Meshfree modeling and homogenization of 3D orthogonal woven composites, Composites Science and Technology 71 (15) (2011) 1777 – 1788.

[28] F. Stig, S. Hallström, A modelling framework for composites containing 3D reinforcement, Composite Structures 94 (9) (2012) 2895 – 2901.

[29] B. Wucher, S. Hallström, D. Dumas, T. Pardoen, C. Bailly, P. Martiny, F. Lani, Nonconformal mesh-based finite element strategy for 3D textile composites, Journal of Composite Materials 51 (16) (2017) 2315–2330.

[30] C. Zhang, J. Curiel-Sosa, T. Q. Bui, Comparison of periodic mesh and free mesh on the mechanical properties prediction of 3D braided composites, Composite Structures 159 (2017) 667 – 676.

[31] T. Huang, Y. Gong, A multiscale analysis for predicting the elastic properties of 3D woven composites containing void defects, Composite Structures 185 (2018) 401 – 410.

[32] M. H. Aliabadi (Ed.), Woven Composites, Vol. 6 of Computational and Experimental Methods in Structures, Imperial College London, UK, 2015.

[33] O. Bacarreza, P. Wen, M. Aliabadi, Micromechanical modelling of textile composites, in: Computational and Experimental Methods in Structures Volume-6 (Woven Composites), Imperial College Press, London, UK, 2015, Ch. 1, pp. 1–74.

[34] N. V. De Carvalho, S. T. Pinho, Mechanical response and failure of 2D woven composites under compression, in: Computational and Experimental Methods in Structures Volume-6 (Woven Composites), Imperial College Press, London, UK, 2015, Ch. 2, pp. 75–107.

[35] S. R. Hallett, S. D. Green, B. S. El Said, Modelling 3D woven composite preform deformations, in: Computational and Experimental Methods in Structures Volume-6 (Woven Composites), Imperial College Press, London, UK, 2015, Ch. 4, pp. 141–158.

[36] L. Kaczmarczyk, C. J. Pearce, N. Bićanić, Scale transition and enforcement of RVE boundary conditions in second-order computational homogenization, International Journal for Numerical Methods in Engineering 74 (3) (2008) 506–522.

[37] X.-Y. Zhou, P. Gosling, C. Pearce, Z. Ullah, L. Kaczmarczyk, Perturbation-based stochastic multi-scale computational homogenization method for woven textile composites, International Journal of Solids and Structures 80 (2016) 368 – 380.

[38] M. Ainsworth, J. Coyle, Hierarchic finite element bases on unstructured tetrahedral meshes, International Journal for Numerical Methods in Engineering 58 (14) (2003) 2103–2130.

[39] Argonne National Laboratory, USA, PETSc Users Manual, 3rd Edition (2018).

[40] T. J. Tautges, I. Grindeanu, R. Jain, D. Wu, The Mesh-Oriented datABase (MOAB), Argonne National Laboratory, USA, 4th Edition (2018).

[41] Trelis 16.5, Sandia National Laboratories, USA, https://www.csimsoft.com/trelis.

[42] ParaView , Open-source, multi-platform data analysis and visualization application, Version 5.4.1, http://www.paraview.org/.

[43] M. Cortis, Numerical modelling of braided fibres for fire resistant fibres reinforced concrete, Ph.D. thesis, School of Engineering, The University of Glasgow, UK (2015).

[44] E. J. Barbero, Finite Element Analysis of Composite Materials, CRC Press Taylor & Francis Group, 2008.

[45] O. Bacarreza, D. Abe, M. H. Aliabadi, N. Kopula Ragavan, Micromechanical modeling of advanced composites, Journal of Multiscale Modelling 04 (02) (2012) 1250005.

[46] A. Cifuentes, A. Kalbag, A performance study of tetrahedral and hexahedral elements in 3-d finite element structural analysis, Finite Elements in Analysis and Design 12 (3) (1992) 313 – 318.

[47] V. Kouznetsova, Computational homogenization for the multi-scale analysis of multi-phase materials, Ph.D. thesis, Technische Universiteit Eindhoven (2002).

[48] C. Miehe, A. Koch, Computational micro-to-macro transitions of discretized microstructures undergoing small strains, Archive of Applied Mechanics 72 (4) (2002) 300–317.